# Domain formation in the type-II/1 superconductor niobium: Interplay of pinning, geometry, and attractive vortex-vortex interaction

Tommy Reimann* and Michael Schulz
*Heinz Maier-Leibnitz Zentrum (MLZ), Technische Universität München, Lichtenbergstr. 1, 85748 Garching, Germany and Physik-Department E21, Technische Universität München, James-Franck-Str. 1, 85748 Garching, Germany*

David F. R. Mildner
*NIST Center for Neutron Research, National Institute of Standards and Technology, Gaithersburg, Maryland 20899, USA*

Markus Bleuel
*NIST Center for Neutron Research, National Institute of Standards and Technology, Gaithersburg, Maryland 20899, USA and Department of Materials Science and Engineering, University of Maryland, College Park, Maryland 20742-2115, USA*

Annie Brûlet
*Laboratoire Léon Brillouin, CNRS-CEA, CEN Saclay, F-91191 Gif-sur-Yvette Cedex, France*

Ralph P. Harti
*Neutron Imaging and Activation Group, Paul Scherrer Institut, 5232 Villigen PSI, Switzerland*

Georg Benka, Andreas Bauer, and Peter Böni
*Physik-Department E21 & 51, Technische Universität München, James-Franck-Str. 1, 85748 Garching, Germany*

Sebastian Mühlbauer†
*Heinz Maier-Leibnitz Zentrum (MLZ), Technische Universität München, Lichtenbergstr. 1, 85748 Garching, Germany*
(Received 18 May 2017; revised manuscript received 4 August 2017; published 10 October 2017)

Vortex attraction which can cause a bundling of vortices has been observed in a multitude of type-II superconductors. While its underlying mechanisms have been extensively studied, the morphology of the emerging vortex superstructure has only been rarely considered. Here, we present a comprehensive experimental study on the type-II/1 superconductor niobium which focuses on the transformation of its homogeneous vortex lattice into an inhomogeneous domain structure at the onset of vortex attraction. By means of small-angle neutron scattering, ultra-small-angle neutron scattering, and neutron grating interferometry, the vortex lattice and the micrometer-scale vortex domain structure as well as its distribution could be investigated. In particular, we focus on the transformation of the vortex lattice at the transition to the intermediate mixed state, which is characterized by vortex attraction. We have found that the phase separation of the vortex lattice into an irregular domain structure takes place via a process showing strong similarity to spinodal decomposition. While pinning disorders the domain morphology, the characteristic length scale of the domain structure is governed by an interplay of field distortion energy and domain surface tension. Finally, geometric barriers in the disk-shaped samples provoke an inhomogeneous distribution of domains on the macroscopic scale.

DOI: 10.1103/PhysRevB.96.144506

## I. INTRODUCTION

Magnetic vortices in type-II superconductors arise in a variety of different configurations including, e.g., liquid, solid, glassy, and amorphous phases. The different manifestations of the vortex state are caused by the multitude of interactions influencing the vortex alignment [1,2]: (i) an intervortex interaction, (ii) correlations with the crystal lattice, (iii) thermal activation, (iv) pinning, and (v) topological restrictions arising from the sample geometry and its boundaries. Depending on the investigated material, these interactions can be of similar magnitude. The complexity of vortex matter is further promoted by the different length scales of these interactions acting on the vortex system: while intervortex interactions and crystal lattice correlations determine the vortex spacing and can affect the crystallography of vortex matter [3], pinning acts collectively on the vortex lattice and can introduce finite correlation lengths to the system [4]. Finally, geometrical effects, including demagnetization and surface, as well as geometrical barriers, cause an inhomogeneous distribution of vortices, predominantly on a macroscopic scale [2,5].

Inconsistent with the Ginzburg-Landau theory [6], which predicts a pure repulsion of vortices, attractive intervortex interaction is frequently observed which perturbs the system further and results in a microscopic domain separation into vortex bundles (Shubnikov domains) and field-free areas (Meissner domains). Although the phenomenon has been known since the 1970s [7], the interest in attractive vortex

*tommy.reimann@frm2.tum.de
†sebastian.muehlbauer@frm2.tum.de

 

interactions has recently resurged, as an unconventional bundling of vortices has been observed in $MgB_2$ and been linked to the two energy bands involved in the superconductivity [8,9]. However, several further mechanisms can provoke a vortex attraction [9]: in the intermediate mixed state (IMS) of type-II/1 superconductors with small Ginzburg-Landau coefficient $\kappa$, the attraction arises from the energy reduction of partially overlaying vortex cores, as has been theoretically derived from the Gor'kov-Eilenberger extensions of the BCS theory [10]. An attractive interaction can furthermore result from a spatial variation of the order parameter, an anisotropy of the superconducting gap, or a layered structure of the superconductor [9,11].

The microscopic origin of vortex attraction and the associated changes of the thermodynamic variables have been the subject of many studies [10,12–14]. In contrast, examinations on the morphology and the evolution of the resulting vortex domain structure are rare and exclusively based on local decoration pictures [7,15], scanning tunneling microscopy [16], and to a lesser extent on small-angle neutron scattering [3,17–20]. Note that also magnetic force microscopy (MFM) [21] and TEM holography [22] can be used for a microscopic access to the vortex morphology. Neither the interplay of vortex attraction and pinning nor the particular impact of the sample geometry have been considered in previous studies, although they crucially determine the final vortex configuration, even far away from the edges of the sample [20]. Moreover, the domain structure of the vortices provides a model case for the investigation of domain formation [20].

Here, we present an experimental study on how the interplay of pinning, geometrical barriers, and vortex attraction governs the process of IMS domain formation in the type-II/1 superconductor niobium. In contrast to previous investigations [20], we concentrate on the process of field cooling, during which the homogeneous vortex lattice decomposes into an inhomogeneous domain structure by the onset of vortex attraction. In order to provide bulk information, this study is based on the combination of neutron grating interferometry (nGI) with small-angle as well as ultra-small-angle neutron scattering (SANS and USANS); details are given in Sec. II.

As a model case of a phase separation process, the transformation of the homogeneous vortex lattice into an IMS domain structure is addressed as a function of the temperature in Sec. III A. A trapping of flux is observed, followed by the subsequent nucleation of an irregular domain structure that is characterized by a defined micrometer correlation length. The presented results suggest that collective pinning weakens at the threshold from repulsive to attractive vortex-vortex interaction. Moreover, the observed phase separation reveals strong similarities to the general process of spinodal decomposition. In Sec. III B, the morphology of the arising domain structure is discussed as a function of the applied magnetic field. An increase of the correlation length with increasing field is found that is explained by the competition of the domains' surface tension and the energy associated with the disturbance of the applied field. While the length scale of the IMS structure is not influenced by pinning, all relevant field scales are reduced compared to pinning free samples. Finally, a pronounced impact of the geometrical barrier is observed, especially for intermediate fields.

## II. EXPERIMENTAL METHODS

The three investigated Nb samples were prepared from the same single-crystal commercially obtained from MaTeck [25]. The concentration of impurities of the crystal has been measured by neutron activation and prompt gamma activation analysis [26]. Hydrogen, tungsten, and tantalum have been tracked as main detectable impurities with a concentration between 200 and 350 ppm each [27]. A list summarizing the shapes, sizes, and demagnetization coefficients $D$ of the investigated samples is given in Table I. The samples were cut with a diamond wire saw and subsequently polished. Two of the samples were finally etched in a mixture of 50% HF and 50% $HNO_3$ for 30 s in order to reduce surface impurities introduced by the cutting and polishing. The samples were prepared with a $\langle 110 \rangle$ direction parallel to the normal vector of the disks and of the largest face of Nb 5. In all measurements, the magnetic field was applied parallel to this crystallographic direction. The Nb wedge and Nb 3 have been used for neutron investigations, while Nb 5 was solely cut for magnetization measurements using a Quantum Design Physical Properties Measurement System (PPMS).

The neutron study on the IMS formation was performed on the SANS instruments SANS-1 at MLZ and TPA at the Laboratoire Léon Brillouin, the USANS beamline BT-5 at the NIST Center for Neutron Research, and the nGI setup at the ANTARES neutron radiography beamline at MLZ. The setups are described by Mühlbauer *et al.* [28], Désert *et al.* [29], Barker *et al.* [30], and Reimann *et al.* [31], respectively. While SANS probes the vortex lattice and permits one to obtain its symmetry and spacing, USANS probes structures on a $\mu$m scale and provides the morphology of IMS domains. Since BT-5 is based on the principle of a Bonse-Hart camera [32], the high reciprocal space resolution is, however, accompanied by a slit smearing of the data. Therefore, USANS does not directly

TABLE I. List of niobium samples. $D$ demagnetization coefficient for the studied field geometry, $r$ radius, and $t$ thickness of the sample.

| Sample | Shape | Dimensions (mm) | Etched | $D$[a] |
|---|---|---|---|---|
| Nb wedge | Disk shaped wedge | $r = 9.3, t = 0.6$–$2.8$ | No | 0.76–0.95 |
| Nb 3 | Disk | $r = 9.3, t = 0.6$ | Yes | 0.95 |
| Nb 5 | Cuboid | $1.9 \times 3.7 \times 4.0$ | Yes | 0.50 |

[a]For the cuboid, $D$ was calculated using the equation given by Aharoni [23], while for the disk samples, it was estimated by approximating the disks as flat ellipsoidals [i.e., $D = 1 - \pi t/(4r)$ [24]]. A definition of the demagnetization coefficient of the wedge is difficult, as an elliptical approximation is not possible, due to the nonparallel surfaces. However, the coefficient should lie between the values of disks with a thickness of 0.6 ($D = 0.95$) and 2.8 mm ($D = 0.76$).

provide the differential scattering cross section $d\sigma/d\Omega$ of the IMS structure, but

$$\left(\frac{d\sigma}{d\Omega}\right)_{\text{slit smeared}}(q) = \frac{1}{q_v}\int_0^{q_v}\frac{d\sigma}{d\Omega}\left(\sqrt{q^2+q_y^2}\right)dq_y, \qquad (1)$$

in which $q_v = 0.117$ Å$^{-1}$ is an instrumental parameter describing the maximum vertical wave vector transfer under which neutrons reach the detector [33]. Finally, nGI produces a spatially resolved map of USANS scattering over the sample and hence records the IMS distribution. Further details on how the obtained data of the three methods are interconnected are given in the Supplemental Material [34].

SANS-1 experiments were conducted using a neutron wavelength of $\lambda = 11.9$ Å ($\frac{\Delta\lambda}{\lambda} = 0.1$) as well as the tightest collimation and maximum sample-to-detector distance of 20 m, respectively. Only the center of the sample was probed by using a 3 mm cadmium mask directly mounted onto the crystal [35].

In contrast, at TPA and BT-5, the beam size was reduced to a diameter of 14 mm in the center of the sample. The experiments were performed with a wavelength of $\lambda = 6$ Å ($\frac{\Delta\lambda}{\lambda} = 0.11$) and $\lambda = 2.38$ Å ($\frac{\Delta\lambda}{\lambda} = 0.06$), respectively.

The nGI results were evaluated from a stepping sequence of the source grating $G_0$ over one complete period in 15 steps. The total exposure time for one dark-field image (DFI) was set to 3000 s. A wavelength of 4.0 Å was used. Due to the bulky sample environment, the spatial resolution of the setup was approximately 0.5 mm.

For all experiments, the sample was mounted in a cryogenic setup providing a base temperature of $T \leqslant 3.7$ K. The sample environment was either a closed cycle cold head cryostat combined with a normal conducting, water cooled magnet in Helmholtz geometry (SANS-1, BT-5, and ANTARES) or a 7 T He bath cryomagnet (TPA). The sample environment was exactly the same at SANS-1 and ANTARES.

## III. RESULTS

In the following section (Sec. III A), the transformation of the homogeneous vortex lattice into an inhomogeneous IMS domain structure is examined as a function of the temperature. Section III B concerns the field dependence of the morphology of the resulting IMS state. As expected for a sample with considerable pinning [36,37], neither USANS nor nGI detected any sign of an IMS nucleation after zero field cooling (ZFC) or high field cooling (HFC), contrary to the presented measurements after field cooling (FC).

### A. IMS domain formation during field cooling in the presence of pinning

#### 1. *Magnetization*

In Fig. 1(a), magnetization data of sample Nb 5 are shown as function of the applied magnetic field for various temperatures between 2 and 9 K. The field was applied after ZFC. Half a hysteresis loop has been measured; hence the data show the initial magnetization curve and the first branch of the irreversible magnetization. The magnetization is negative after the initial field ramp and positive in decreasing fields. For all

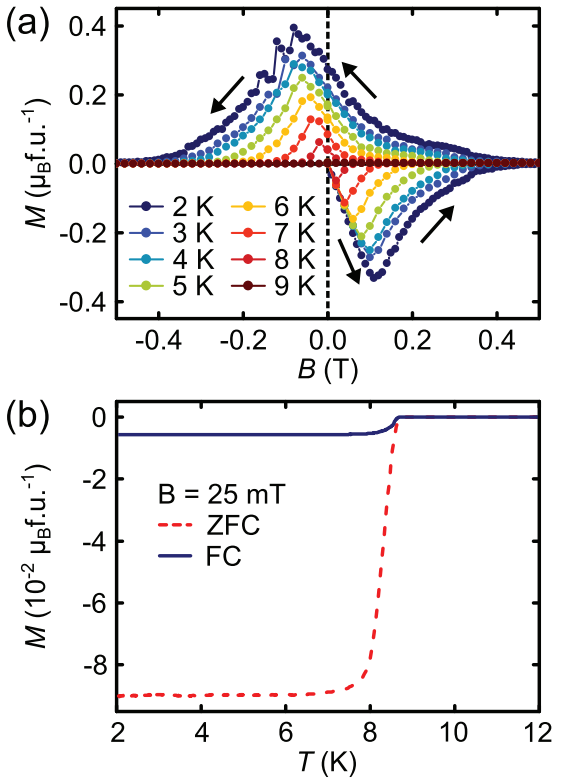


FIG. 1. Magnetization data of the cuboid sample Nb 5. (a) Magnetization as function of the applied magnetic field, measured for different temperatures between 2 and 9 K. Shown are the initial magnetization curve after ZFC and half a hysteresis loop. (b) Temperature dependence of the magnetization at $B = 25$ mT. The curve was measured once for increasing temperatures, after ZFC to 2 K, and successive application of the magnetic field, and once for decreasing temperature in an applied field (FC).

temperatures, the remanent magnetization at 0 T is roughly 2/3 of the maximum $M(B)$ value.

The upper critical field $B_{C2}(T)$ is marked by the disappearance of the magnetization, since normal conducting Nb is only slightly diamagnetic. At 4 K, $B_{C2}$ is determined to be 420 mT which is considerably higher than values reported in literature for pure Nb [e.g., $B_{C2}^{\text{Lit}}(4.2\text{ K}) = 275$ mT [38]]. The critical temperature is obtained to be $T_C = 9.1 \pm 0.1$ K by extrapolating the upper critical field $B_{C2}(T)$ to zero [39]. This value is only slightly reduced compared to pure samples ($T_C^{\text{Lit}} = 9.3$ K [14]). The broad hysteresis, the high remanence, and the increase of $B_{C2}$, as well as the degradation of $T_C$, demonstrate the high impact of impurities and pinning on the properties of the studied crystal.

As expected [37], a determination of $B_{C1}$ is thus not possible from the kink in the $M(B)$ data set, as the field of first flux penetration is strongly increased by pinning. Accordingly, also the IMS transition, which would appear as a kink in $M(B)$ in pinning free samples with finite demagnetizing factor (see Fig. 3 of Ref. [2]) is masked by bulk pinning in our sample. Moreover, the hysteresis loops also indicate that volume pinning is dominant over surface and edge (geometrical) barriers. For the latter, the magnetization becomes reversible for low inductions [2,40]. Similarly, geometrical barriers less

affect flux exit as compared to flux entry, leading to strongly skewed hysteresis loops [40]. In particular, no hints of any IMS domain formation can be drawn from magnetization data $M(B)$.

Typical $M(T)$ data are presented in Fig. 1(b) for an applied field of 25 mT. The red dashed curve was measured for increasing temperatures after initial zero field cooling of the sample. In contrast, the blue curve was measured FC, i.e., for decreasing temperature in an applied field. In a pinning free sample, both curves would overlap (neglecting geometrical barriers [5]), since the thermodynamic equilibrium is reached independent of the cooling path. Moreover, the magnetization would continuously decrease with decreasing temperature, since the sample becomes more diamagnetic [41]. In contrast, the examined Nb sample is less diamagnetic after FC, as pinning prevents a complete expulsion of magnetic flux during cooling. Furthermore, the magnetization is temperature independent in most of the superconducting phase. Deviations from a constant magnetization emerge above 6.3 K and 7.8 K for ZFC and FC measurements, respectively. Interestingly, a reversible state where both curves coincide is not found below $T_C(25\ \text{mT}) = 8.8$ K, underlining that the studied situation does not correspond to the thermodynamic equilibrium.

For field cooling and field heating paths, the signature of an IMS transition is less obvious as compared to $M(B)$. In particular, both the equilibrium induction inside the vortex domains [19,42] and the associated filling factor of the sample change with temperature. Up to now, the impact of IMS domain formation on the magnetization for FC paths has not been treated theoretically. In general, as mentioned in the previous paragraph, samples with and without pinning expel the magnetic flux on cooling in field [41], depending on the pinning strength. The saturation of the magnetization $M(T)$ observed over a wide temperature range strongly suggests that the vortex configuration is frozen on a FC path and is in line with prominent pinning. A frozen state of the vortex lattice, however, seems incompatible with the formation of a spatially inhomogeneous IMS state.

### 2. *Small-angle neutron scattering*

As a next step, bulk magnetization data are compared to the local magnetic induction $B_{\text{int}}$ within the vortex lattice that is measured by means of small-angle neutron scattering.

Typical SANS results obtained on the Nb wedge are presented in Fig. 2(a). The scattering pattern corresponds to the sum of a rocking scan performed after the sample had been field cooled in an applied field of 41 mT. The data have been normalized to zero field; hence only magnetic contributions are visible. A clear scattering pattern, characteristic of a long range ordered vortex lattice, emerges, whose hexagonal symmetry for fields along the ⟨110⟩ direction is in agreement with literature [3]. The temperature dependence of the reciprocal lattice spacing of the vortex lattice, $g_{\text{VL}}$, is shown in Fig. 2(b) for three different values of the magnetic field. $g_{\text{VL}}$ is inverse to the vortex lattice parameter $a_{\text{VL}}$:

$$g_{\text{VL}} = \frac{4\pi}{\sqrt{3}a_{\text{VL}}} = \sqrt{\frac{8\pi^2 B_{\text{int}}}{\sqrt{3}\Phi_0}}, \tag{2}$$

in which $\Phi_0$ is the magnetic flux quantum.

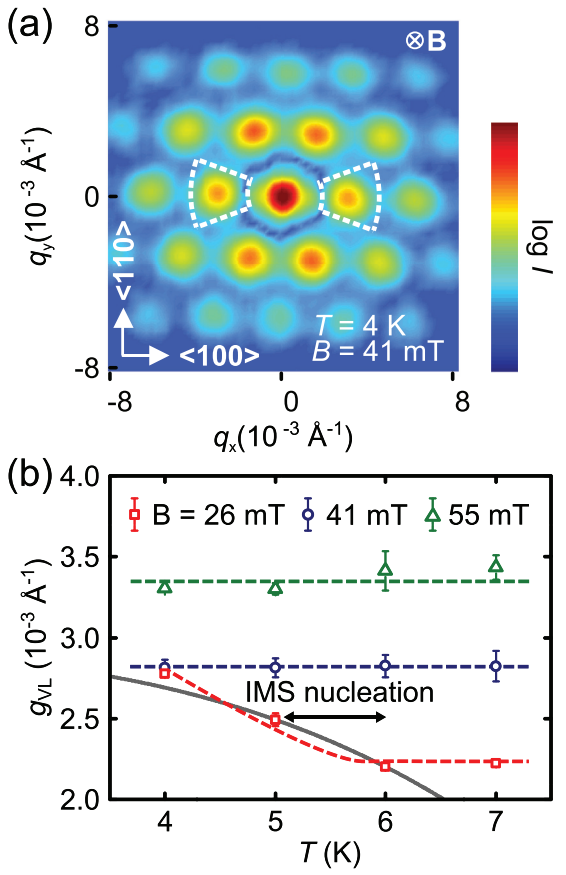


FIG. 2. Results of the niobium wedge obtained at SANS-1. (a) Typical SANS pattern of the vortex lattice in Nb. (b) Quantitative evaluation of the reciprocal vortex lattice spacing $g_{\text{VL}}$ which corresponds to the position of the horizontal first order Bragg peaks [marked in (a)]. $g_{\text{VL}}$ is drawn as function of the temperature for three different field values. The error bars correspond to the differences of the spacing extracted from the left and the right peaks. These errors are slightly larger than the errors associated with the determination of the peak position.

At 55 and 41 mT, $g_{\text{VL}}$ assumes a constant value of $3.4\times10^{-3}$ and $2.8\times10^{-3}$ Å$^{-1}$, respectively. No variation of the lattice parameter is detected for 7 K $\geqslant T \geqslant$ 4 K, in agreement with magnetization measurements suggesting a frozen state of the vortex lattice below 7 K. However, cooling in a field of 26 mT is accompanied by a continuous increase of $g_{\text{VL}}$ from $2.2\times10^{-3}$ Å$^{-1}$ to $2.8\times10^{-3}$ Å$^{-1}$ below 6 K. Hence the local magnetic induction within the flux line lattice, as given by Eq. (2), strongly increases from 22 mT to 36 mT. In contrast to the bulk magnetization, which indicates a static arrangement of flux in this temperature regime for 25 mT [Fig. 1(b)], SANS clearly shows a microscopic rearrangement of the vortex lattice below 6 K. In particular, the SANS experiment shows a constant, field-independent vortex lattice parameter $g_{\text{VL}}$ at 4 K for 26 and 41 mT, which is the hallmark of an IMS domain structure.

In contrast to the temperature dependence of $g_{\text{VL}}$ during the IMS transition, a detailed analysis of the SANS pattern did not show any signature in the longitudinal, transverse, and orientational correlation lengths as extracted from the width of

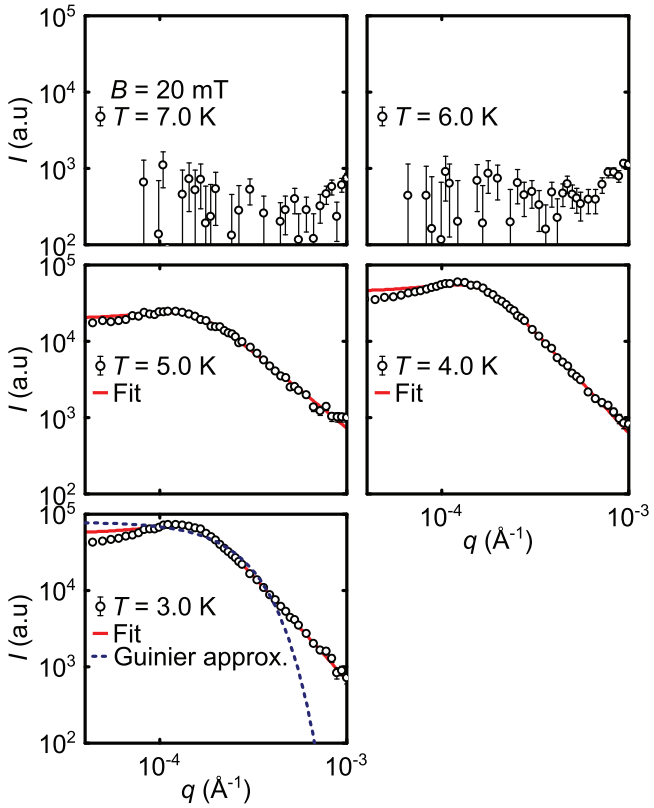


FIG. 3. USANS scattering curves at $B = 20$ mT for various temperatures after FC. The data are normalized to curves above $T_C$. Data were taken on the Nb wedge. $B$ was applied along ⟨110⟩, parallel to the neutron beam, while the crystallographic ⟨100⟩ direction was rotated into the horizontal plane. Pronounced scattering can only be detected below 6 K. The red line is a fit to Eq. (3). Shown are statistical error bars.

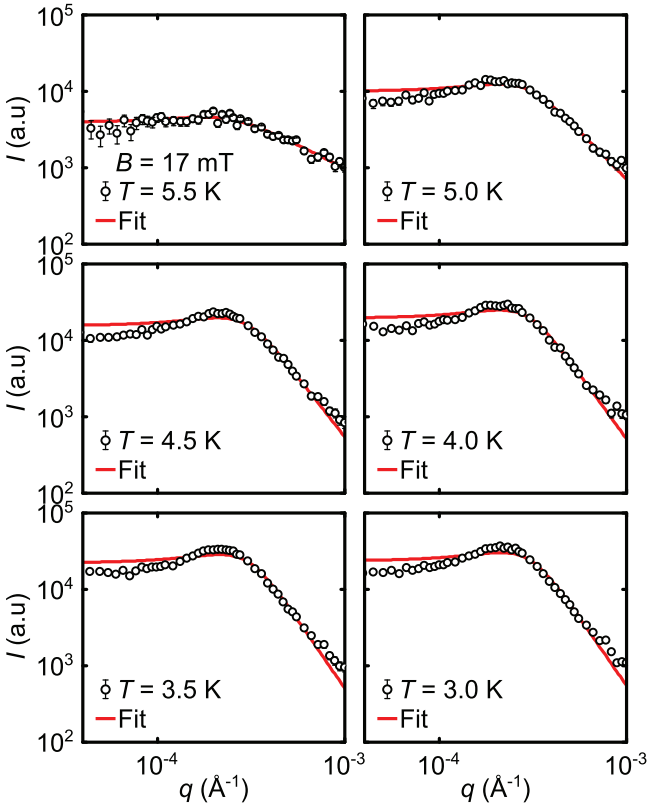


FIG. 4. USANS scattering curves at $B = 17$ mT for various temperatures after FC. The data are normalized to curves above $T_C$. Data were taken on the Nb wedge. $B$ was applied along ⟨110⟩, parallel to the neutron beam, while the crystallographic ⟨100⟩ direction was rotated into the horizontal plane. The red line is a fit to Eq. (3). Shown are statistical error bars.

the rocking scans, $Q$ scan, and azimuthal scan [43]. However, due to the rather low momentum transfer $Q$, the resolution of the SANS experiment is poor. In addition, no significant loss of integrated intensity of the vortex lattice Bragg peaks is observed at the transition to the IMS. This rules out a transition to a mostly disordered state of the vortex lattice since such a configuration does not yield a coherent scattering pattern at all [44]. Note that only the central part of the sample was exposed to neutrons for the SANS experiment.

### 3. *Ultra-small-angle neutron scattering*

In contrast to indirect evidence obtained by SANS, the formation of the IMS domain structure itself can be directly traced using ultra-small-angle neutron scattering. Typical USANS rocking curves are shown in Figs. 3 and 4 for a magnetic field of 20 and 17 mT, respectively. Plotted is the scattered intensity as a function of the wave vector transfer $q$. The data was measured during FC from 10 to 4 K. Data were taken on the Nb wedge. Only magnetic scattering is present, since the scattering curves were normalized to data above $T_C$.

At 20 mT (Fig. 3), no signal is found for 6 K $\leqslant T \leqslant$ 7 K. Only at high $q$, a weak onset of a peak appears that is attributed to the Bragg peak of the vortex lattice at $g_{\mathrm{VL}}$ which is slightly above the probed $q$ range [19]. For $T < 6$ K, pronounced USANS scattering develops that is characterized by a peak around $1.2\times10^{-4}$ Å$^{-1}$, corresponding to a correlation length of $\approx 2$ $\mu$m, and a decreasing intensity following a power law for high $q$. The position of the peak remains nearly constant in the probed temperature range. However, the scattered intensity strongly increases with decreasing temperature.

Similar behavior is found for $B = 17$ mT (Fig. 4) which has been measured with finer temperature steps. The peak is found at approximately $2.8\times10^{-4}$ Å$^{-1}$. Again, the scattered intensity significantly increases for decreasing temperature. Furthermore, the width of the peak seems to decrease moderately by lowering $T$.

In both cases, the occurrence of a correlation peak confirms that, below 6 K, a magnetic (super)structure emerges within the sample that is characterized by a particular correlation length in the micrometer range. Together with the indirect evidence observed by SANS, measurements with USANS clearly reveal that a microscopic rearrangement of the vortex system to an IMS domain structure takes place below 6 K.

### 4. *Modeling of the USANS data: Phase separation at the transition to the IMS*

Further information about the structural changes of the vortex system at the transition to the IMS can be obtained by

modeling of the USANS data. This requires a smearing of the particular model function according to Eq. (1). While earlier decoration experiments on pure Nb particularly found laminar as well as tubular domain morphologies [9], the scattering data could neither be described by the corresponding cylindrical nor by laminar form factors [45] which directly follows from the lack of a Guinier behavior [46] at low $q$, exemplarily shown in Fig. 3 for 3 K. However, a sufficient agreement with the data has been obtained by slit smearing [Eq. (1)] of the empirical scattering function given by Furukawa [47]:

$$I_{\text{unsmeared}}(q) = I_{\max}\frac{\left(1+\frac{\gamma_s}{2}\right)\left(\frac{q}{q_{\max}}\right)^2}{\frac{\gamma_s}{2}+\left(\frac{q}{q_{\max}}\right)^{2+\gamma_s}}, \tag{3}$$

where $q_{\max}$ is the position of a correlation peak and $I_{\max}$ is its corresponding intensity. The parameter $\gamma_s$, describing the power law decrease at high $q$ values, is connected to the dimensionality of the system [47]. This scattering function is typically used to describe phase-separating mixtures that develop during spinodal decomposition [48]. Hence the underlying model describes an irregular, isotropic two-phase system which is characterized by a preferred correlation length.

Fits of the data to Eq. (3) are shown as red lines in Figs. 3 and 4. The scattering curves are sufficiently approximated by the fit, but small deviations occur at low and high $q$ values. Deviations at large $q$ are attributed to the vortex lattice Bragg peak at $g_{\text{VL}}$. The discrepancy at small $q$ could indicate a slight anisotropy of the scattering function that is not covered by Eq. (3).

The resulting correlation length $q_{\max}$, characterizing the microstructure, and the intensity $I_{\max}$ are plotted as function of temperature in Figs. 5(a) and 5(b). While $q_{\max}$ is temperature independent (with the exception of 5.5 K at 17 mT), the intensity $I_{\max}$ continuously increases with decreasing temperature. Since the shape of the scattering curve only changes little, the increase of intensity can be attributed to (i) an enhancement of scattering length density contrast between Shubnikov and Meissner domains or (ii) a growth of the number of domains.

The scattering length density depends on the difference between the induction within the Shubnikov domains $B^{\text{IMS}}(T) \propto (g_{\text{VL}}^{\text{IMS}}(T))^2$ and the macroscopic mean induction $\overline{B}$. The latter is proportional to the square of the reciprocal vortex lattice spacing $(g_{\text{VL}}(T = 7\text{ K}))^2$ since below, the flux is macroscopically trapped. The intensity variation due to the changed scattering contrast will therefore increase as:

$$I_{\max} \propto \left[\left(g_{\text{VL}}^{\text{IMS}}(T)\right)^2 - (g_{\text{VL}}(T = 7\text{ K}))^2\right]^2. \tag{4}$$

Recently, Pautrat [19] has found that the temperature dependence of the vortex lattice parameter within the IMS of Nb can be sufficiently described by $a_{\text{VL}} \propto (1 - t^{3-t})^{-1/2}$, in which $t = T/T_{\text{C}}$. This behavior arises because $a_{\text{VL}}$ is mainly influenced by the change of the London penetration depth [49]. Accordingly, $I_{\max}$ should vary as

$$I_{\max} = A_{\text{U}}[A_{\text{S}}(1 - t^{3-t}) - (g_{\text{VL}}(T = 7\text{ K}))^2]^2, \tag{5}$$

in which $A_{\text{U}}$ and $A_{\text{S}}$ are fit parameters. Because $T_{\text{C}}$, $A_{\text{S}}$, and $g_{\text{VL}}(T = 7\text{ K})$ can be directly determined from magnetization and SANS data, Eq. (5) has only one free parameter. Fits of $I_{\max}$ to Eq. (5) for 17 and 20 mT are shown in Fig. 5(b). The

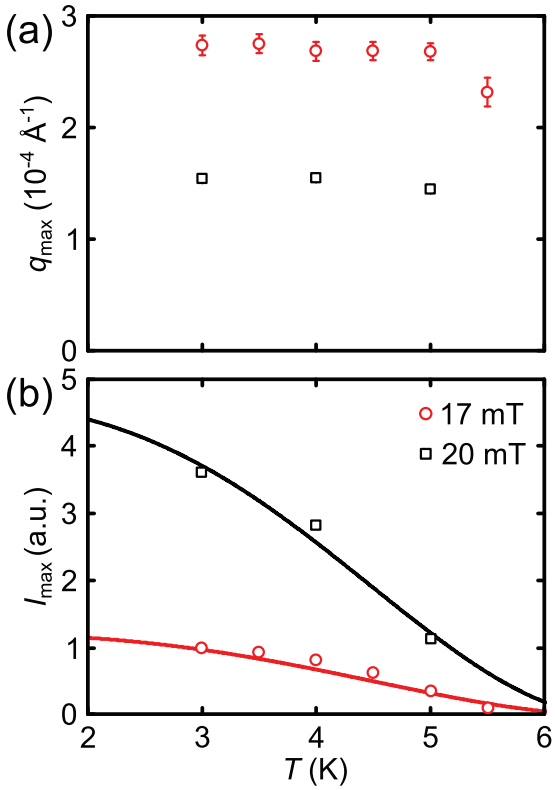


FIG. 5. Quantitative evaluation of the USANS data shown in Figs. 4 and 3. (a) Maximum of the scattering curves $q_{\max}$ as function of the temperature. The maximum is nearly temperature independent. Only for 17 mT, the peak is slightly shifted to lower $q$ at 5.5 K. The error bars for 20 mT lie within the symbols. (b) Temperature dependence of the parameter $I_{\max}$ for 17 and 20 mT, extracted from the USANS scattering curves. The solid lines are fits to Eq. (5).

corresponding approximation of $g_{\text{VL}}^{\text{IMS}}(T)$ is drawn as a gray line in Fig. 2(b). Although the number of data points is clearly too low for a quantitative evaluation, the agreement of the fits to the USANS data is gratifying. The increasing intensity with decreasing temperature seen by USANS can hence be very likely attributed to the change of scattering length density contrast in the IMS microstructure.

In conclusion, our SANS and USANS measurements have unambiguously shown the formation of an inhomogeneous IMS state from a homogeneous vortex lattice phase upon field cooling. This requires a microscopic rearrangement of vortices. In contrast, bulk magnetization shows a frozen arrangement of flux caused by pinning in this temperature window. Most astonishingly, SANS clearly shows a formation of an IMS domain structure for the central part of the sample, hence in a region presuably unaffected by vortex gradients alongside of the Bean model. However, caused by the poor resolution of the SANS experiment, no microscopic details of this rearrangement process are yet available: no loss of transverse, longitudinal, or azimuthal correlation or of intensity of the *ordered* part of the vortex lattice domains could be observed. This indicates that the vortex lattice within the IMS domains is well ordered and shows a unique alignment of the symmetry axes with respect to the crystalline orientation throughout the sample. Our data can be fitted with an empirical

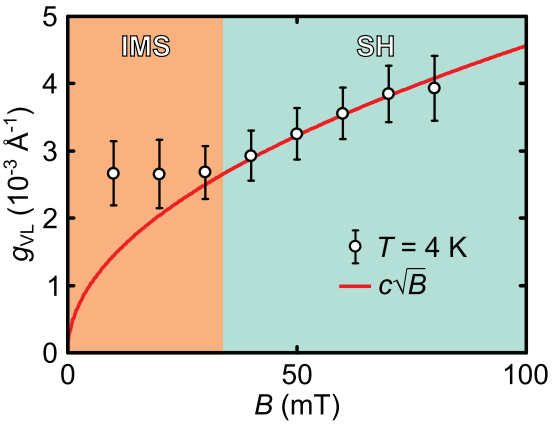


FIG. 6. SANS results of Nb 3 measured at TPA. Shown is the position of the first order vortex lattice Bragg peak $g_{VL}$ as a function of the applied magnetic field. The data were obtained after field cooling to $T = 4$ K. Error bars correspond to the standard deviation. In low fields, the sample is in the IMS, and the typical constant $q$ behavior is observed. In higher fields, $g_{VL}$ is proportional to $\sqrt{B}$, characteristic of the Shubnikov phase (SH).

function resembling a spinodal decomposition with a fixed correlation length. The increasing scattering contrast can be explained by the temperature dependent magnetic contrast of the IMS domains.

### B. Morphology of the IMS after field cooling as a function of the applied field

In the following section, the field dependence of the IMS domain structure that emerges upon field cooling is systematically studied by means of SANS, USANS, and nGI in order to (i) uncover the physical origin of the correlation length found in the IMS microstructure, (ii) detect the influence of pinning on the IMS field range, and (iii) reveal the further impact of geometric effects on the IMS distribution.

#### 1. Small-angle neutron scattering

The field range of the IMS phase can be deduced by SANS. It is connected to the lower critical field $B_{C1}$ and the local induction within the IMS $B_0$ via [18,38]

$$(1 - D)B_{C1} \leqslant B \leqslant (1 - D)B_{C1} + DB_0 = B_2. \quad (6)$$

SANS results obtained at TPA on the sample Nb 3 are presented in Fig. 6. Shown is $g_{VL}$ as function of the magnetic field after the sample has been field cooled to $T = 4$ K for various magnetic fields. The data have been obtained similar to the ones shown in Fig. 2(b). The hallmark of the IMS [17], a constant $g_{VL}$, is observed below 40 mT. In higher fields, $g_{VL}$ is proportional to $\sqrt{B}$ as indicated by the red line shown in the figure. The transition from the IMS to the Shubnikov phase at $B_2$ can be deduced from the intersection of the high field curve with the constant $q$ value of the IMS. Since this constant value $g_{VL}^{IMS}$ is furthermore connected to the induction within the Shubnikov domains $B_0$ via Eq. (2), the lower critical field $B_{C1}$ can be calculated from these quantities [Eq. (6)]. Values for $g_{VL}^{IMS}$, $B_2$, $B_0$, and $B_{C1}$ are summarized in Table II. These values are considerably reduced compared to pure Nb [3,20],

TABLE II. Reciprocal lattice parameter $g_{VL}^{IMS}$ of the vortex lattice within the IMS, field of the IMS to Shubnikov transition $B_2$, induction within the Shubnikov domains $B_0$, and lower critical field $B_{C1}$ of the sample Nb 3.

| $g_{VL}^{IMS}$ ($10^{-3}$ Å) | $B_2$ (mT) | $B_0$ (mT) | $B_{C1}$ (mT) |
|---|---|---|---|
| $2.6 \pm 0.1$ | $34 \pm 1$ | $32 \pm 1$ | $72 \pm 20$ |

where comparable $B_{C1}$ values are found around $T = 7$ K [50]. The configuration of the vortex lattice on a field cooling path is hence strongly influenced by pinning and the corresponding freezing transition.

#### 2. Ultra-small-angle neutron scattering

A detailed investigation of the IMS domain morphology nucleating during FC was performed using USANS. Typical rocking curves for field cooling to 4 K in different applied fields between 9 and 51 mT are shown in Fig. 7 (Nb 3 disk). Presented is the scattered intensity as a function of the wave vector transfer $q$. The data were normalized to zero field.

A distinct magnetic scattering signal, indicating the presence of IMS domains, was found for all investigated fields. Similar to Fig. 3, the scattering curves are distinguished by a power law decrease at high $q$. In comparison to the Nb wedge, for which a clear correlation peak is observed, the peak is washed out and remains as a kink in the data for the Nb 3 disk sample. With increasing magnetic field, the kink position continuously moves to lower $q$ values while the overall scattered intensity increases up to 26 mT and decreases above. Even at the highest fields of 43 and 51 mT, a scattering signal is still observed, although the kink seems to have moved below the momentum range probed by USANS. A qualitatively similar magnetic field dependence is found for the Nb wedge (see Supplemental Material [51]).

#### 3. IMS domain structure described by the models of Landau and Goren-Tinkham

In order to obtain further information on the field dependence of the IMS morphology, the scattering curves of Fig. 7 were modeled according to Eq. (3). Corresponding fits to the data are shown as red lines in Fig. 7. The scattering curves are well approximated by the fit indicating that the kink in the data results from the slit smearing of a scattering function with a correlation peak (see Supplemental Material [54]). Above 43 mT, an accurate fitting of the data is hampered by the missing kink. Describing the high $q$ behavior arising from scattering at the surface of the IMS domains [55], the parameter $\gamma_s$ is deduced to be $\gamma_s \approx 3$, which is expected for scattering off a two dimensional structure below the percolation threshold of multiple domains [48]. A slight decrease (to $\gamma_s \approx 2.5$) is found for high fields, in line with an elongation or a coalescence of the domain structure.

The position of the correlation peak $q_{max}$ as extracted by fitting the data to Eq. (3) is plotted as function of the magnetic field in Fig. 8. It is inverse to the correlation length $a$ which characterizes the IMS microstructure ($a = 2\pi/q_{max}$).

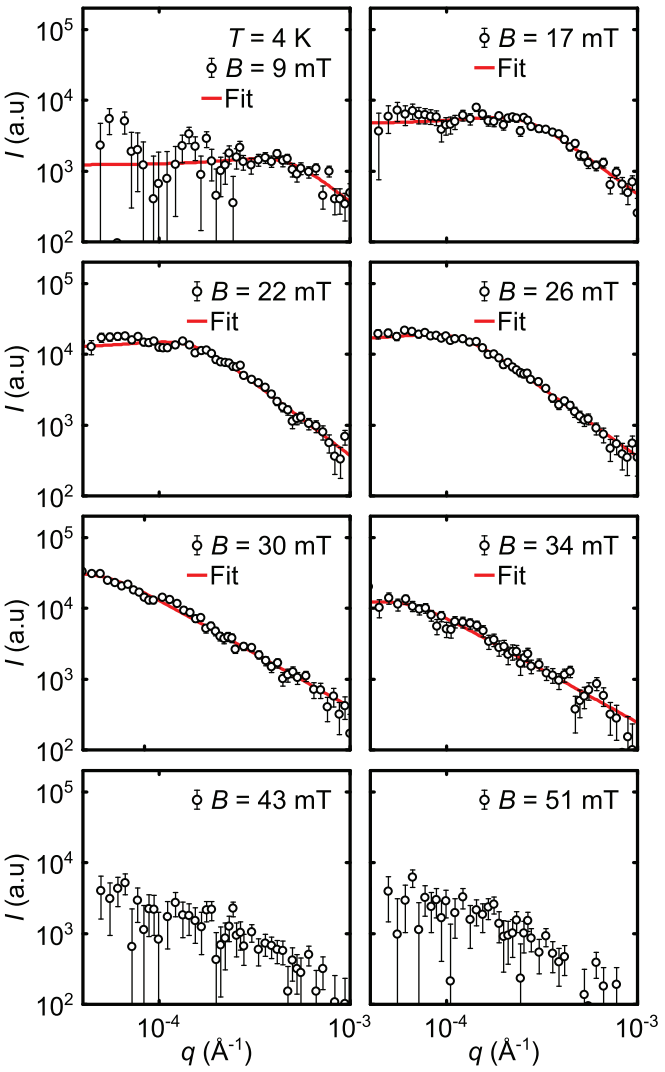


FIG. 7. USANS scattering curves of Nb 3 for different magnetic fields. The sample has been field cooled to 4 K. $B$ was applied along ⟨110⟩, parallel to the neutron beam, while another crystallographic ⟨110⟩ direction was rotated into the horizontal plane. The red curves are fits to Eq. (3). Shown are statistical error bars.

The correlation length continuously increases with increasing field, attributed to growing Shubnikov domains.

In order to qualitatively describe the field dependence of the correlation length, the data have been compared to the models of Landau [52] as well as of Goren-Tinkham [53], which have been originally proposed to describe the domain size found in the intermediate state (IS) of type-I superconductors. In these frameworks, the domain size results as an interplay between the surface energy (tension) of the domains and the energy attributed to the field distortion caused by the domain formation. Assuming a laminar domain pattern, Landau found for the field dependence [56]

$$a = \left[\frac{\delta t b}{f_{\mathrm{L}}(b)}\right], \tag{7}$$

in which $\delta$ is the superconducting wall-energy parameter, $t$ the sample thickness, and $f_{\mathrm{L}}$ a numerical function tabulated in Ref. [57]. In contrast, by assuming a hexagonal tubular

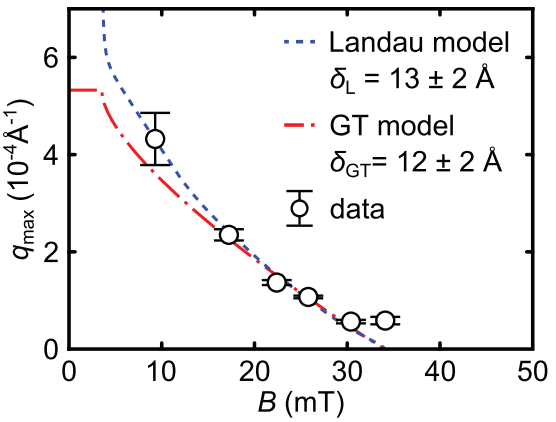


FIG. 8. Field dependence of the domain size. The graphs show the parameter $q_{\mathrm{max}}$, extracted from USANS, as a function of the magnetic field for the sample Nb 3. Error bars correspond to the uncertainty of the fit. The red dashed-dotted and blue dashed curves correspond to fits to the Landau [52] and the Goren-Tinkham [53] model.

structure, Goren and Tinkham derived [53]

$$a = \sqrt{\frac{2\delta t}{(1-b)(1-\sqrt{b})}}. \tag{8}$$

With $b = B/B_{\mathrm{C}}$, both models have been successfully applied to describe the IS domain patterns found in various type-I superconductors, though it has been realized that the models are oversimplified and the domain morphologies may be further changed by small additional effects like pinning or geometrical restrictions [58,59].

Both models can be used to interpret our data on the IMS structure of type-II superconductors. However, for such materials the superconducting surface energy is negative and does not govern the domain size. Instead, the surface energy of the Shubnikov domains results as a cleavage energy of the vortex lattice due to the vortex attraction. The wall-energy parameter $\delta$ is thus a measure of the strength of the vortex bonds [7,60]. Finally, in order to incorporate demagnetization effects, an adaption of $b$ is necessary:

$$b = \frac{B - (1-D)B_{\mathrm{C1}}}{DB_0}, \tag{9}$$

since, within the IMS, the domain volume fraction is expected to increase linearly with the field [17]. As long as $D$ is close to unity, as it is assumed in the original models of Landau and Goren-Tinkham, the used model is valid. Fits of $q_{\mathrm{max}}$ to Eqs. (7) and (8) are shown as blue dashed and red dotted-dashed curves in Fig. 8, respectively. Here, $B_0$, $B_{\mathrm{C1}}$, $D$, and $t$ have been taken from Tables II and I, respectively. Thus only the wall-energy parameter $\delta$ remained undefined. Its values, extracted via the Landau and the Goren-Tinkham approaches, are $\delta_{\mathrm{L}} = 13 \pm 2$ Å and $\delta_{\mathrm{GT}} = 12 \pm 2$ Å, respectively. Both models approximate the data well. Only for 34 mT does the obtained correlation length lie above the model functions, since this field corresponds to the upper boundary of the IMS determined by SANS.

A more detailed determination of the domain morphology from the field dependence of the domain size is not possible,

since (i) the errors in $q_{max}$ are too large as to allow for an unambiguous attribution of the domain size behavior to a specific model and (ii) the IMS morphology is not expected to be characterized by either the pure laminar or tubular patterns underlying the models. Nonetheless, the determined wall-energy parameter $\delta \approx 12 \pm 4$ Å is rather independent of the used model and comparable to values which can be calculated from the results given in Refs. [7,60]. The data thus confirms that the correlation length of the IMS microstructure arises from the competition of surface tension and field distortion and seems not explicitly influenced by pinning.

#### *4. Neutron grating interferometry*

Besides the microscopic influence of pinning, the impact of geometrical barriers on the IMS nucleation on the macroscopic scale has recently been demonstrated [20]. The distribution of the IMS during domain nucleation has hence been probed by means of nGI. Corresponding data of the Nb wedge are presented in Fig. 9. The sample has been field cooled to 5 K in different applied magnetic fields. The dark-field images (DFI) have been normalized to zero field; hence only magnetic contrast is visible. In order to eliminate the implicit dependence of the DFI contrast on the sample thickness $t$, the dark-field images presented in Fig. 9 have been corrected for each pixel $(j,l)$ according to [61]

$$\mathrm{DFI}_{\mathrm{cor}}(j,l) = \mathrm{DFI}(i,j)^{\frac{1}{t(j,l)}}, \tag{10}$$

in which $t(j,l)$ is the normalized thickness of the wedge-shaped sample at position $(j,l)$. Positions within the sample revealing a low DFI value correspond to positions where neutrons are strongly scattered off IMS domains. Hence nGI is directly sensitive to the spatial distribution of IMS domains within the sample. Further details on the DFI contrast modality are given in the Supplemental Material.

A DFI signal indicating the presence of an IMS domain structure is found for fields $7\ \mathrm{mT} \leqslant B \leqslant 35\ \mathrm{mT}$. Below 15 mT, the DFI contrast is essentially homogeneous over the whole sample. However, as a main result of the measurement, a strongly inhomogeneous contrast develops for $15 \leqslant B \leqslant 25$ mT. Corresponding DFIs are characterized by a low value in the center of the sample and a minimum on a ring close to the sample's edge. Above 29 mT, this peculiar DFI variation vanishes, and the contrast is essentially homogeneous apart from a small vertical gradient which arises from a slightly off-centered positioning of the disk in the magnetic field. For all fields, the DFI signal starts to continuously increase already ∼2 mm inside the edge. In summary, our data show that the IMS domain structure which forms from a homogeneous vortex lattice phase upon field cooling is inhomogeneously distributed over the sample. The inhomogeneity is attributed to geometrical barriers.

## IV. DISCUSSION

In our study, we have obtained a consistent description of the nucleation of a spatially inhomogeneous IMS domain structure emerging from a homogeneous vortex lattice phase in the presence of pinning and geometrical effects under field cooling. In contrast, for zero field cooling or high field cooling, no signs of domain formation have been observed experimentally. This can be readily understood in the framework of the critical state theory [36,37]: the field gradients which develop in order to move the flux front within the sample seem incompatible to the formation of vortex clusters. In the following paragraphs, we disentangle the multitude of different influences acting on the vortex lattice upon field cooling in detail.

### A. Vortex lattice freezing transition caused by pinning

For $10\ \mathrm{K} \geqslant T \geqslant 7\ \mathrm{K}$, the sample enters the Shubnikov phase from the normal conducting state. As expected, the magnetic field is macroscopically expelled from the sample with decreasing temperature as seen by magnetization measurements [Fig. 1(b)]. In this temperature window, pinning only acts weakly on the vortices. Microscopically, the vortex

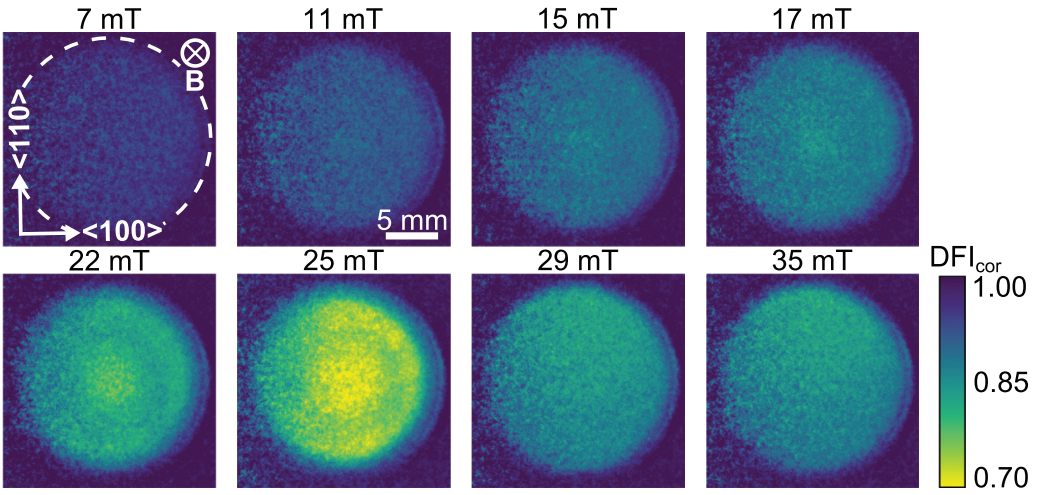


FIG. 9. Results of nGI on the Nb wedge at a temperature of 5 K in different magnetic fields applied before cooling. The wedge thickness increases from left to right, which causes an increased noise on the left of the images. The shown DFI have been normalized to zero field and corrected for the sample thickness according to Eq. (10). The sample position is indicated by the white circle. A low DFI value corresponds to a high amount of USANS scattering off the IMS arising from the corresponding position within the sample.

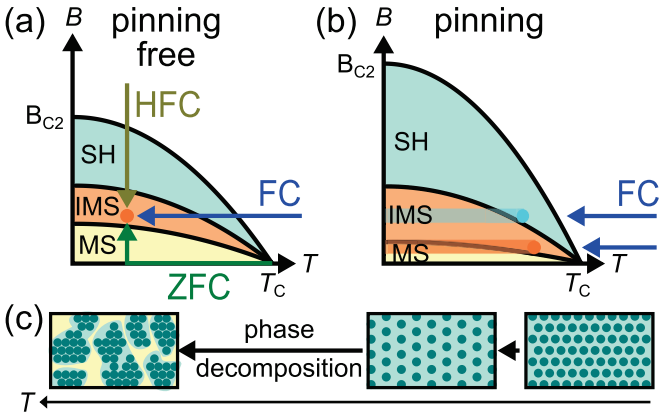


FIG. 10. Schematic phase diagram of Nb for the pure and pinning free sample (a), and for the samples revealing significant pinning (b). In the absence of pinning, the vortex lattice reaches the thermodynamic equilibrium independent of the field and temperature history (under the assumption that geometrical barriers are negligible). In contrast, pinning prevents the sample from reaching equilibrium, and metastable states are frozen during FC. This is exemplarily sketched by the horizontal orange and blue streaks in (b). (c) Evolution of the vortex lattice during field cooling.

lattice spacing is expected to increase in this temperature regime upon cooling as it has been observed for pure niobium samples (Fig. 11 of Ref. [42]).

In the region 6 K $\leqslant T \leqslant$ 7 K $= T_{\mathrm{F}}$, the material has been cooled below a freezing temperature $T_{\mathrm{F}}$ at which the vortex lattice is pinned within the material. The expulsion of flux is stopped, indicated by the constant values for $M(T)$ [Fig. 1(b)] and $g_{\mathrm{VL}}$ probed by SANS (Fig. 2). As a consequence the magnetic properties of the sample can be described using the critical state model [36] which assumes that the flux lines can only be moved along a field gradient sufficiently high to overcome the pinning forces. Effects of field cooling on the macroscopic field distribution have been treated in Refs. [41,62]. Although geometrical effects had been neglected in these works, it has been shown that during field cooling the induction within a superconductor is only reduced along a small area near the edge of the sample, while it is unaffected in its center. This behavior is in accordance with the presented data.

As a direct consequence, besides a depleted area near the edge of the sample, the magnetic flux within the sample thus does not correspond to the equilibrium induction for low temperatures, but to the value trapped within the sample at higher temperatures (around 6 to 7 K). In particular, the deduced $B_{\mathrm{C1}}(T = 4\ \mathrm{K})$ corresponds to a value found for ~7 K in pure materials. Consistently, SANS and USANS as well as nGI show that all relevant field scales for the IMS phase are considerably reduced compared to pure samples. The situation is schematically sketched in Fig. 10.

### B. Breakdown of pinning at the onset of vortex attraction

However, for $T \leqslant 6\ \mathrm{K} = T_{\mathrm{IMS}}$, the vortex lattice changes on a microscopic scale. (i) Its lattice parameter is reduced as indicated by SANS and (ii) a magnetic $\mu$m domain superstructure nucleates as shown by USANS. The change of the vortex lattice is striking, since the macroscopic magnetization is unaffected. Moreover, SANS clearly shows that the vortex lattice in the central part of the sample is affected, hence far away from regions affected by vortex gradients of the Bean model. Pinning within the sample therefore prevents a further expulsion of the vortex lattice through the depleted zone, but not an internal rearrangement of it. This observation underlines that pinning forces interact collectively with the elastic vortex lattice and not merely on individual vortices [4].

Microscopically, the elastic properties of the vortex lattice are strongly influenced at the transition from vortex repulsion to vortex attraction. In particular, a hardening of the elastic tilt modulus of the vortex lattice has been measured [42]. While for pure niobium this transition has been predicted [10] and observed [13] very close to $T_{\mathrm{C}}$, it is considerably shifted to lower temperatures in the present samples, due to their high impurity content and the connected higher $\kappa$ [10]. The presented data show that for a magnetic field of $B \approx$ 20 mT the transition from a repulsive to an attractive vortex-vortex interaction occurs around 6 K. Only the weakening or breakdown of collective pinning allows for the observed microscopic rearrangement of vortices. For higher magnetic fields above the IMS (41 and 55 mT), the vortex lattice parameter stays constant and no domains nucleate.

### C. Interplay of pinning, vortex attraction, and magnetic field energy on the IMS morphology

A pronounced influence of pinning is observed on the IMS domain morphology. The presented USANS data suggest an irregular, isotropic two-phase mixture rather than the generic tubular or laminar patterns previously observed in very pure samples [9]. A similar strong distortion of vortex domains due to the presence of pinning has been predicted by molecular-dynamics simulations on attracting vortices exposed to quenched disorder [63–65].

During field cooling, the correlation length characterizing the IMS domain structure and the shape of the scattering curve is mostly temperature independent over the probed $T$ range [Fig. 5(a)], indicating that the morphology of the microstructure does not strongly vary. Moreover, the concentration of vortices within the Shubnikov domains continuously increases with temperature as seen using SANS [Fig. 2(b)], leading to an increasing field gradient within the IMS microstructure, in line with the growing USANS intensity.

A phase transformation from the Shubnikov to the IMS via a nucleation and growth process cannot account for these observations. The scattering curve can however be well approximated by a model function introduced for the investigation of spinodal decomposition in metal alloys [48]. The strong similarity of the IMS domain nucleation to a spinodal decomposition is furthermore strengthened by the following findings: during FC, the equilibrium vortex system is frozen into a metastable state due to the onset of pinning which then becomes unstable with the transition to an attractive vortex-vortex interaction. Moreover, in the critical state model, pinning supports the development of vortex gradients [36,37]. Finally, during IMS formation, a temperature independent correlation length of the IMS is observed. The magnetic field dependence of $q_{\mathrm{max}}$ shows that this correlation length

is determined by the interplay of domain surface energy and magnetic field energy. In contrast to classical phase ordering processes, the IMS phase separation can rather be controlled by temperature and field than by time. Microscopically, SANS indicates a well defined positional order of the vortices in the IMS domains throughout the sample.

### D. Influence of geometrical barriers on the IMS distribution

We finally address the macroscopic inhomogeneity revealed by the nGI experiments. On this scale, more subtle influences of geometric effects on the IMS formation are observed. Its main manifestations are as follows. (i) A reduced DFI contrast near the edge of the sample for all fields, in line with flux depletion explained by the critical state model on type-II superconductors [41]. (ii) An unexpected, inhomogeneous contrast variation of the signature of the IMS domain structure deep within the sample at intermediate fields (see Supplemental Material).

It seems likely that this inhomogeneity is caused by the geometrical barrier [2] within the disk shaped sample, since (i) its impact is strongest for intermediate fields, which is a hallmark of geometrical barriers [66], and (ii) the DFI contrast variation strongly resembles the ones obtained on the IS of lead in the presence of a geometrical barrier [66,67]. However, to fully account for the special situation of type II superconductors, further continuum electrodynamics computations in line with Refs. [68,69] are necessary in order to simulate the field distribution during field cooling in samples with considerable pinning.

## V. SUMMARY

In conclusion, we have presented a comprehensive bulk investigation on the interplay of pinning, sample geometry, and attractive vortex interactions on the IMS formation in the type-II/1 superconductor niobium. By means of SANS, USANS, and nGI, the vortex lattice and the micrometer-scale vortex domain structure as well as its distribution could be studied while crossing the transition from repulsive to attractive vortex interactions. In particular, we have found that pinning disorders the domain morphology and changes the phase separation towards a process showing strong resemblance to spinodal decomposition in two dimensions. However, the characteristic length scale of the domain structure is still governed by the interplay of domain surface tension and magnetic field energy, and is not influenced by pinning. On the macroscopic length scale, geometrical barriers cause local inhomogeneities in the IMS domain structure which are pronounced for intermediate fields. Finally, further high resolution SANS measurements to elucidate the microscopic properties of the IMS transition and the corresponding correlation lengths including the Larkin length remain as a task for future studies. In particular, position resolved measurements should clarify the microstructure of the different regions as observed with nGI.

While the presented study concentrates on type-II/1 superconductors, the obtained information on the influence of pinning and sample geometry are independent of the specific origin of the microscopic vortex attraction. In the presence of pinning, a similar process of cluster formation is therefore expected in various other type-II materials sharing the crossover to a partial vortex attraction as common property. As a practical impact, our work clearly shows that, in the presence of pinning, a dramatic change of the superconducting vortex lattice can even occur deep inside a bulk sample without signature in bulk magnetization measurements. Finally, the similarity of the phase separation observed in the IMS to decomposition processes found in various metal alloys, glasses, and polymers again underlines the model character of vortex matter for the investigation of general effects arising in solid state physics.

## ACKNOWLEDGMENTS

We are very grateful to Alan Ye (NIST) for his excellent technical support during the USANS measurements, to Zsolt Révay, Christian Stieghorst, and Alexander Backs for providing us with the PGAA results of the Nb samples, as well as to Christian Grünzweig for fruitful discussions. This project has received funding from the European Union's 7th Framework Programme for research, technological development, and demonstration under the NMI3-II Grant No. 283883. Financial support by the Deutsche Forschungsgemeinschaft (DFG) through TRR80 (project E1) is gratefully acknowledged. Access to the USANS instrument was provided by the Center for High Resolution Neutron Scattering, a partnership between the National Institute of Standards and Technology and the National Science Foundation under Agreement No. DMR-0944772.

[1] G. Crabtree and D. Nelson, Phys. Today **50**, 38 (1997).
[2] E. H. Brandt, Rep. Prog. Phys. **58**, 1465 (1995).
[3] S. Mühlbauer, C. Pfleiderer, P. Böni, M. Laver, E. M. Forgan, D. Fort, U. Keiderling, and G. Behr, Phys. Rev. Lett. **102**, 136408 (2009).
[4] A. I. Larkin and Y. N. Ovchinnikov, J. Low Temp. Phys. **34**, 409 (1979).
[5] E. Zeldov, A. I. Larkin, V. B. Geshkenbein, M. Konczykowski, D. Majer, B. Khaykovich, V. M. Vinokur, and H. Shtrikman, Phys. Rev. Lett. **73**, 1428 (1994).
[6] V. L. Ginzburg and L. D. Landau, Zh. Eksp. Teor. Fiz. **20**, 1064 (1950).
[7] U. Krägeloh, Phys. Status Solidi B **42**, 559 (1970).
[8] V. Moshchalkov, M. Menghini, T. Nishio, Q. H. Chen, A. V. Silhanek, V. H. Dao, L. F. Chibotaru, N. D. Zhigadlo, and J. Karpinski, Phys. Rev. Lett. **102**, 117001 (2009).
[9] E. H. Brandt and M. P. Das, J. Supercond. Novel Magn. **24**, 57 (2011).
[10] U. Klein, J. Low Temp. Phys. **69**, 1 (1987).
[11] A. I. Buzdin, A. S. Mel'nikov, A. V. Samokhvalov, T. Akashi, T. Masui, T. Matsuda, S. Tajima, H. Tadatomo, and A. Tonomura, Phys. Rev. B **79**, 094510 (2009).
[12] J. Auer and H. Ullmaier, Phys. Rev. B **7**, 136 (1973).

[13] H. Weber, E. Seidl, M. Botlo, C. Laa, E. Mayerhofer, F. Sauerzopf, R. Schalk, H. Wiesinger, and J. Rammer, Phys. C (Amsterdam, Neth.) **161**, 272 (1989).

[14] H. Weber, E. Seidl, M. Botlo, C. Laa, H. Wiesinger, and J. Rammer, Phys. C (Amsterdam, Neth.) **161**, 287 (1989).

[15] C. Herring, Phys. Lett. A **47**, 103 (1974).

[16] J.-Y. Ge, J. Gutierrez, A. Lyashchenko, V. Filipov, J. Li, and V. V. Moshchalkov, Phys. Rev. B **90**, 184511 (2014).

[17] D. K. Christen, F. Tasset, S. Spooner, and H. A. Mook, Phys. Rev. B **15**, 4506 (1977).

[18] D. K. Christen, H. R. Kerchner, S. T. Sekula, and P. Thorel, Phys. Rev. B **21**, 102 (1980).

[19] A. Pautrat and A. Brûlet, J. Phys.: Condens. Matter **26**, 232201 (2014).

[20] T. Reimann, S. Mühlbauer, M. Schulz, B. Betz, A. Kaestner, V. Pipich, P. Böni, and C. Grünzweig, Nat. Commun. **6**, 8813 (2015).

[21] H. Yang, B. Shen, Z. Wang, L. Shan, C. Ren, and H.-H. Wen, Phys. Rev. B **85**, 014524 (2012).

[22] J. E. Bonevich, K. Harada, H. Kasai, T. Matsuda, T. Yoshida, and A. Tonomura, Phys. Rev. B **50**, 567 (1994).

[23] A. Aharoni, J. Appl. Phys. **83**, 3432 (1998).

[24] C. Poole, H. Farach, R. Creswick, and R. Prozorov, *Superconductivity* (Elsevier Science, Amsterdam, 2010).

[25] Certain commercial equipment, instruments, or materials are identified in this paper to foster understanding. Such identification does not imply recommendation or endorsement by the National Institute of Standards and Technology, nor does it imply that the materials or equipment identified are necessarily the best available for the purpose.

[26] Z. Révay, P. Kudějová, K. Kleszcz, S. Söllradl, and C. Genreith, Nucl. Instrum. Methods Phys. Res. A **799**, 114 (2015).

[27] Oxygen, which is expected to be present in the material as well, is not traceable by this method.

[28] S. Mühlbauer, A. Heinemann, A. Wilhelm, L. Karge, A. Ostermann, I. Defendi, A. Schreyer, W. Petry, and R. Gilles, Nucl. Instrum. Methods Phys. Res. A **832**, 297 (2016).

[29] S. Désert, V. Thévenot, J. Oberdisse, and A. Brûlet, J. Appl. Crystallogr. **40**, s471 (2007).

[30] J. G. Barker, C. J. Glinka, J. J. Moyer, M. H. Kim, A. R. Drews, and M. Agamalian, J. Appl. Crystallogr. **38**, 1004 (2005).

[31] T. Reimann, S. Mühlbauer, M. Horisberger, B. Betz, P. Böni, and M. Schulz, J. Appl. Crystallogr. **49**, 1488 (2016).

[32] U. Bonse and M. Hart, Appl. Phys. Lett. **7**, 238 (1965).

[33] S. R. Kline, J. Appl. Crystallogr. **39**, 895 (2006).

[34] See Supplemental Material at http://link.aps.org/supplemental/10.1103/PhysRevB.96.144506 for further details and Refs. [70–84] therein.

[35] Experiments performed with the masked placed closer to the sample edge did not qualitatively change the results.

[36] C. P. Bean, Phys. Rev. Lett. **8**, 250 (1962).

[37] T. Matsushita, *Flux Pinning in Superconductors*, Springer Series in Solid-State Sciences (Springer, Heidelberg, 2014).

[38] H. R. Kerchner, D. K. Christen, and S. T. Sekula, Phys. Rev. B **21**, 86 (1980).

[39] M. Tinkham, Phys. Rev. **129**, 2413 (1963).

[40] R. Prozorov, Phys. Rev. Lett. **98**, 257001 (2007).

[41] J. R. Clem and Z. Hao, Phys. Rev. B **48**, 13774 (1993).

[42] S. Mühlbauer, C. Pfleiderer, P. Böni, E. M. Forgan, E. H. Brandt, A. Wiedenmann, U. Keiderling, and G. Behr, Phys. Rev. B **83**, 184502 (2011).

[43] M. R. Eskildsen, E. M. Forgan, and H. Kawano-Furukawa, Rep. Prog. Phys. **74**, 124504 (2011).

[44] T. Klein, I. Joumard, S. Blanchard, J. Marcus, R. Cubitt, T. Giamarchi, and P. Le Doussal, Nature (London) **413**, 404 (2001).

[45] J. Kohlbrecher, Sasfit: A program for fitting simple structural mmodel to small angle scattering data, online, https://kur.web.psi.ch/sans1/SANSSoft/sasfit.html, 2012.

[46] A. Guinier, G. Fournet, C. B. Walker, and G. H. Vineyard, Phys. Today **9**, 38 (1956).

[47] H. Furukawa, Physica A: Stat. Mech. Appl. **123**, 497 (1984).

[48] H. Furukawa, Adv. Phys. **34**, 703 (1985).

[49] B. Mühlschlegel, Z. Phys. **155**, 313 (1959).

[50] D. K. Finnemore, T. F. Stromberg, and C. A. Swenson, Phys. Rev. **149**, 231 (1966).

[51] See Supplemental Material at http://link.aps.org/supplemental/10.1103/PhysRevB.96.144506 for USANS Data for Nb wedge.

[52] L. D. Landau, Nature (London) **141**, 688 (1938).

[53] R. N. Goren and M. Tinkham, J. Low Temp. Phys. **5**, 465 (1971).

[54] See Supplemental Material at http://link.aps.org/supplemental/10.1103/PhysRevB.96.144506 for a comparison of the smeared and unsmeared scattering curve.

[55] G. Porod, Kolloid-Z. **124**, 83 (1951).

[56] L. D. Landau, Zh. Eksp. Teor. Fiz. **7**, 371 (1937).

[57] J. Sykes, D. Haar, and L. Pitaevskii, *Perspectives in Theoretical Physics: The Collected Papers of E. M. Lifshitz* (Elsevier Science, Amsterdam, 2012).

[58] R. Choksi, V. R. Kohn, and F. Otto, J. Nonlin. Sci. **14**, 119 (2004).

[59] J. R. Clem, R. Prozorov, and R. J. Wijngaarden, Phys. Rev. B **88**, 104504 (2013).

[60] T. Reimann, Ph.D. thesis, TU München, 2017.

[61] M. Strobl, Sci. Rep. **4**, 7243 (2014).

[62] S. L. Li, H. H. Wen, and Z. X. Zhao, Phys. C (Amsterdam, Neth.) **316**, 293 (1999).

[63] C. Reichhardt, J. Drocco, C. J. Olson Reichhardt, and A. R. Bishop, Physica C: Supercond. **479**, 15 (2012).

[64] X. B. Xu, H. Fangohr, Z. H. Wang, M. Gu, S. L. Liu, D. Q. Shi, and S. X. Dou, Phys. Rev. B **84**, 014515 (2011).

[65] H. J. Zhao, V. R. Misko, and F. M. Peeters, New J. Phys. **14**, 063032 (2012).

[66] R. Prozorov, R. W. Giannetta, A. A. Polyanskii, and G. K. Perkins, Phys. Rev. B **72**, 212508 (2005).

[67] T. Reimann, M. Schulz, C. Grünzweig, A. Kaestner, A. Bauer, P. Böni, and S. Mühlbauer, J. Low Temp. Phys. **182**, 107 (2016).

[68] E. H. Brandt, Phys. Rev. B **58**, 6506 (1998).

[69] E. H. Brandt, Phys. Rev. B **59**, 3369 (1999).

[70] C. Grünzweig, F. Pfeiffer, O. Bunk, T. Donath, G. Kühne, G. Frei, M. Dierolf, and C. David, Rev. Sci. Instrum. **79**, 053703 (2008).

[71] C. Grünzweig, Ph.D. thesis, ETH Zürich, 2009.

[72] F. Pfeiffer, O. Bunk, C. Schulze-Briese, A. Diaz, T. Weitkamp, C. David, J. F. van der Veen, I. Vartanyants, and I. K. Robinson, Phys. Rev. Lett. **94**, 164801 (2005).

[73] W. Yashiro, Y. Terui, K. Kawabata, and A. Momose, Opt. Express **18**, 16890 (2010).

[74] S. K. Lynch, V. Pai, J. Auxier, A. F. Stein, E. E. Bennett, C. K. Kemble, X. Xiao, W.-K. Lee, N. Y. Morgan, and H. H. Wen, Appl. Opt. **50**, 4310 (2011).
[75] T. Donath, M. Chabior, F. Pfeiffer, O. Bunk, E. Reznikova, J. Mohr, E. Hempel, S. Popescu, M. Hoheisel, M. Schuster, J. Baumann, and C. David, J. Appl. Phys. **106**, 054703 (2009).
[76] S. W. Lee, D. S. Hussey, D. L. Jacobson, C. M. Sim, and M. Arif, Nucl. Instrum. Methods Phys. Res. A **605** 16 (2009).
[77] A. Hilger, N. Kardjilov, T. Kandemir, I. Manke, J. Banhart, D. Penumadu, A. Manescu, and M. Strobl, J. Appl. Phys. **107**, 036101 (2010).
[78] J. Kim, S. W. Lee, and G. Cho, Nucl. Instrum. Methods Phys. Res. A **746**, 26 (2014).
[79] R. Andersson, L. F. van Heijkamp, I. M. de Schepper, and W. G. Bouwman, J. Appl. Crystallogr. **41**, 868 (2008).
[80] J. Schelten and W. Schmatz, J. Appl. Crystallogr. **13**, 385 (1980).
[81] F. Mezei, C. Pappas, and T. Gutberlet, *Neutron Spin Echo Spectroscopy: Basics, Trends and Applications*, Lecture Notes in Physics (Springer, Heidelberg, 2008).
[82] B. Betz, R. P. Harti, M. Strobl, J. Hovind, A. Kaestner, E. Lehmann, H. Van Swygenhoven, and C. Grünzweig, Rev. Sci. Instrum. **86**, 123704 (2015).
[83] M. Strobl, B. Betz, R. P. Harti, A. Hilger, N. Kardjilov, I. Manke, and C. Gruenzweig, J. Appl. Crystallogr. **49**, 569 (2016).
[84] S. Gkoumas, P. Villanueva-Perez, Z. Wang, L. Romano, M. Abis, and M. Stampanoni, Sci. Rep. **6**, 35259 (2016).